## Probing Nuclear Interactions Through Isotope Shift Spectroscopy of Mercury

Thorsten Groh,\* Felix Affeld, and Simon Stellmer Physikalisches Institut, Universität Bonn, Nussallee 12, 53115 Bonn, Germany (Dated: October 23, 2025)

We present precision isotope shift spectroscopy of the  $6s^2 \, ^1S_0 \rightarrow 6s \, 6p \, ^3P_1$  intercombination line and the  $6s \, 6p \, ^3P_1 \rightarrow 6s \, 6d \, ^3D_J$  (J=1,2) transitions in neutral mercury, performed on the five naturally abundant even isotopes, including the low-abundant isotope  $^{196}$ Hg. Using laser-cooled atoms in a magneto-optical trap, we achieve uncertainties down to  $20 \, \text{kHz}$ , resolving the isotope shifts to a fractional uncertainty of  $\sim 2 \times 10^{-6}$ . A King plot analysis comparing our  $^1S_0 \rightarrow ^3P_1$  data to previous results on the  $6s \, 6p \, ^3P_2 \rightarrow 6s \, 7s \, ^3S_1$  line reveals a nonlinearity with  $4.9 \, \sigma$  significance. Our generalized King plot nonlinear decomposition analysis discusses potential contributions from quadratic ( $\propto \delta \langle r^2 \rangle^2$ ) and higher order field shifts ( $\propto \delta \langle r^4 \rangle$ ) also induced by nuclear deformations. These measurements yield new insights into the structure of the Hg nucleus and provide benchmarks for nuclear-structure models. They further establish mercury as a potential platform to search for hypothetical Yukawa-type boson-mediated forces coupling electrons to neutrons.

High-precision, low-energy experiments now reach extraordinary accuracy, with optical clocks operating at the  $10^{-18}$  level [1–3], hydrogen spectroscopy testing theory at  $10^{-15}$  [4, 5], and the electron g-factor known at the level of  $10^{-13}$  [6, 7], enabling stringent tests of fundamental symmetries, dark matter searches, and searches for variations of fundamental constants [8–10].

Recently, isotope shift spectroscopy (ISS) has emerged as a key probe at the interface of atomic, nuclear, and particle physics [11–21]. In particular, ISS provides sensitivity to beyond standard model (BSM) parityconserving electron-neutron interactions, mediated by hypothetical light bosons [22, 23]. This search is also motivated by the reported 17 MeV <sup>8</sup>Be anomaly, interpreted as a potential vector boson [24, 25]. Such interactions are inaccessible to collider experiments, but could manifest as nonlinearities in King plot (KP) analyses of ISs [26]. Recent high-resolution IS measurements in calcium (Ca) and ytterbium (Yb) provide strong bounds on a Yukawa-type electron-neutron interaction across boson masses from 10 to  $10^7 \,\mathrm{eV}/c^2$  [11–16, 19, 27, 28] and exclude wide regions of parameter space associated with extended Higgs sectors, alternative mass-generation mechanisms, and light mediators [22]; with bounds now comparable to astrophysical and other constraints [6, 29–33].

Isotope shift—The IS,  $\delta \nu_i^{A-A'} \equiv \nu_i^A - \nu_i^{A'}$ , is the change in the frequency  $\nu_i$  of an electronic transition i between isotopes of mass numbers A and A'. To leading order perturbation theory, we can write

$$\delta\nu_i^{A-A'} = F_i \,\delta\langle r^2 \rangle^{A-A'} + K_i \,\delta\mu^{A-A'} + \sum_{\kappa} G_i^{(\kappa)} \,\delta\eta_{(\kappa)}^{A-A'}, \ (1)$$

where  $F_i$ ,  $K_i$  and  $G_i^{(\kappa)}$  denote transition dependent electronic and the  $\delta x^{A-A'} \equiv x^A - x^{A'}$  nuclear factors [26].

In heavy elements like mercury (Hg), the IS is dominated by the field shift (FS), which is proportional to the difference in mean-square nuclear charge radii  $\delta \langle r^2 \rangle^{A-A'} \equiv \langle r^2 \rangle^A - \langle r^2 \rangle^{A'}$ . Originating from the overlap of the electronic wavefunction with the nuclear charge

distribution, it is strongest for s-electrons: in Hg, the 6s<sup>2</sup> ground state largely determines the IS of the intercombination line [34, 35]. The mass shift (MS), arising from the nuclear recoil, is proportional to the inverse nuclear mass difference,  $\delta \mu^{A-A'} \equiv 1/m^A - 1/m^{A'}$ . It approximately scales as  $1/(m^A)^2$ , making it strongest in the hydrogendeuterium IS and dominates the IS in light systems, such as Ca, while being strongly suppressed in Hg [36].

The terms  $\delta\eta^{A-A'}_{(\kappa)}$  denote higher order (nuclear) corrections. For heavy elements, higher order nuclear moments, like the quadratic FS (QFS)  $\propto \delta(\langle r^2 \rangle^2)^{A-A'}$ , are expected to be the next resolvable contributions [11]. Recent ISS measurements in Yb ions on the sub-hertz level [11–16] have revealed nuclear deformation (ND) contributions  $\propto \delta \langle r^4 \rangle^{A-A'}$  (= quartic FS [15]) reflecting prolate deformation of the nuclear charge distribution limiting BSM searches [26]. By contrast, the near-spherical nuclei of Ca suppress such corrections: early measurements confirmed linearity [17, 18], while combined Ca<sup>+</sup> and Ca<sup>14+</sup> spectroscopy later uncovered a significant KP nonlinearity consistent with second-order mass shift (MS)  $\propto 1/(m^A)^2 - 1/(m^{A'})^2$  and nuclear polarization (NP) effects [19], the latter being a subtle electron interaction induced deformation of the nuclear charge distribution. For certain transitions, second-order FS or MS effects mix nearby levels, yielding large IS corrections [37] that produced up to 32 MHz shifts in samarium [38–40].

Despite these SM contributions, ISS can be used to probe for a new physics boson  $\phi$  coupling neutrons to electrons via a Yukawa-like interaction,  $V_{\rm NP}(r) = -\alpha_{\rm NP} \, (A-Z) \, e^{-m_\phi \, r} / r \, [22,\,41]$ . This interaction introduces a term  $\propto \alpha_{\rm NP} \, X_i \, \gamma^{A-A'}$  that only depends on the difference in the number of neutrons,  $\gamma^{A-A'} = (A-A')$ . Precision ISS can place bounds on the electron to neutron coupling strength  $\alpha_{\rm NP} = (-1)^s \, \gamma_e \, \gamma_n$  and the mediator mass  $m_\phi \, [22,\,23]$ .

Mercury—Hg (Z=80) provides a system capturing the strengths of Ca and Yb. Its nuclei are close to spherical due to the nearby proton shell closure at Z=82

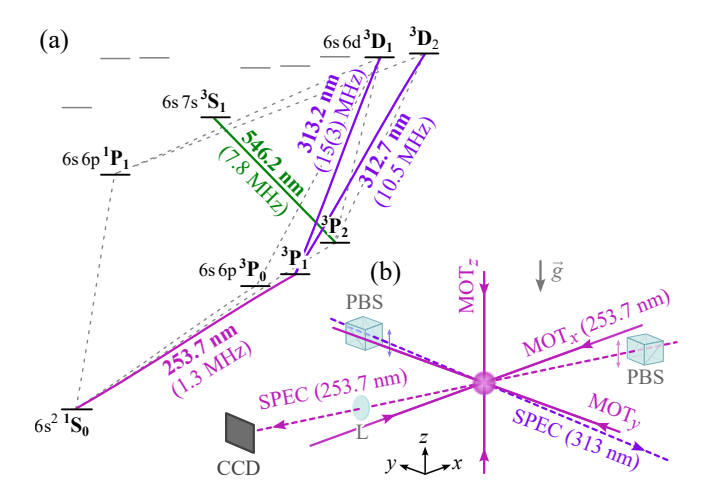


FIG. 1. (a) Level scheme of Hg relevant for isotope shift spectroscopy within this work (natural linewidths given in brackets). (b) Experimental setup for spectroscopy of the  ${}^{1}S_{0} \rightarrow {}^{3}P_{1}$  intercombination line at 253.7 nm and the  ${}^{3}P_{1} \rightarrow {}^{3}D_{J}$  lines at 313.2 nm (J=1) and 312.7 nm (J=2). Atoms are cooled in a MOT at 253.7 nm. For resolving the  ${}^{1}S_{0} \rightarrow {}^{3}P_{1}$  line, atoms are probed in free fall via absorption imaging at 253.7 nm. The light is vertically polarized via a polarization beam splitter (PBS), propagates in the xy-plane and is imaged on a UV-sensitive charge-coupled device (CCD) sensor via a single objective lens (L). For resolving the  ${}^{3}P_{1} \rightarrow {}^{3}D_{J}$  lines, vertically polarized light at 313 nm depletes the MOT atom number via optical pumping and subsequent decay to  ${}^{3}P_{0,2}$  and  ${}^{1}P_{1}$  (gray, dashed lines). Atom numbers within the MOT are then determined by fluorescence imaging at 253.7 nm.

and neutron shell closure at N=126, reducing nuclear deformation-driven contributions [42, 43], while the large nuclear charge Z enhances sensitivity to electron–neutron couplings. Hg provides narrow optical clock transitions and five stable even-even isotopes (see Tab. I), enabling high-precision ISS and KP analysis. Hg IS measurements range from early arc spectra and vapor cell studies [44– 48] to very recent comb-referenced Doppler-free saturation spectroscopy experiments at sub-MHz [49] and down to kHz-level [50, 51] precision. Apart from searches for new forces, Hg spectroscopy benchmarks nuclear structure through precise charge radii, exhibiting features like the kink at N = 126 and shape staggering in neutrondeficient isotopes [52]. Atomic beam and collinear laser ISS established charge radii and magnetic dipole and electric quadrupole moments of <sup>181</sup>Hg to <sup>206</sup>Hg [53], recent studies at ISOLDE extended these measurements to isotopes as light as <sup>177</sup>Hg, revealing pronounced odd-even staggering consistent with shape coexistence [54–58].

Experiment—We probe the IS of neutral Hg atoms on three distinct dipole-allowed lines in a magneto-optical trap (MOT) as illustrated in Fig. 1. The setup is similar to the one described in Ref. [59]. For the most abundant  $^{202}$ Hg, we load up to  $N=1\times 10^7$  atoms from a background gas and cool them to  $T\approx 150\,\mu\text{K}$ .

The ultraviolet (UV) spectroscopy light is derived via frequency conversion from an infrared (IR) externalcavity diode laser at  $1015\,\mathrm{nm}~(\nu \to 4\,\nu)$  and  $1565\,\mathrm{nm}$  $(\nu \to 5 \nu)$  respectively. The quintupled 313 nm laser system is similar to the setup described in Ref. [60] and generates about 1 mW of stable laser power in the UV. We lock the fundamental wavelength of the spectroscopy lasers to a length-stabilized ultra-low expansion (ULE) cavity (finesse  $\mathcal{F} = 74\,100(660)$  at  $1015\,\mathrm{nm}$  and  $\mathcal{F} = 166\,460(350)$  at 1565 nm), which acts as the frequency reference for ISS. A fiber electro-optic modulator shifts the laser frequency relative to the cavity resonances to address individual isotopes. For  ${}^{1}S_{0} \rightarrow {}^{3}P_{1}$ , where the IS spans about 20 GHz in the UV and exceeds the free spectral range (FSR) of the cavity ( $\delta_{\rm FSR}$  = 2992455.6(3) kHz), we lock the master laser to the nearest cavity resonance. We characterize the ageing of the cavity spacer as a linear drift in time using repeated measurements of the  $^1{\rm S}_0 {\to}^3{\rm P}_1$  transition. A simultaneous fit,  $\delta^A_{\rm cav}(t) = n_{\nu}\,a_{\rm cav}\,t + \delta^{\star A}_{\rm cav}$ , to all isotopes gives  $a_{\rm cav} = -0.200(4)\,{\rm Hz/s}$  (at 1015 nm) and the driftcorrected atomic resonance  $(\nu_0^A)$  to cavity reference line detuning  $\delta_{\text{cav}}^{\star A} \equiv \nu_0^A - n_\nu \, \nu_{\text{cav},0}$ , where  $n_\nu = 4 \, (n_\nu = 5)$  denotes the conversion factor from IR to UV. acousto-optic modulators in the UV scan the probe beam detuning  $\Delta$ across the atomic linewidth and control the beam power. All RF frequencies are phase locked to a 10 MHz Rb microwave clock reference.

For spectroscopy of the  $^1\mathrm{S}_0 \rightarrow ^3\mathrm{P}_1$  intercombination line at 253.7 nm, where we also operate the MOT, we probe the atoms in free fall via absorption imaging. We switch off both the magnetic gradient field and the cooling light and spectroscopically address the atoms with a probe beam intensity of  $s_0 = I/I_{\mathrm{sat}} \approx 0.02$  for an exposure time of  $t_{\mathrm{exp}} = 150\,\mathrm{\mu s}$ .

For the  ${}^3\mathrm{P}_1 \rightarrow {}^3\mathrm{D}_J$  lines, we instead keep the MOT cooling light on, which populates the excited  ${}^3\mathrm{P}_1$  state. Atom numbers are then determined via their fluorescence at 253.7 nm. Probe light at 313 nm ( $s_0 \approx 0.03$ ) optically pumps excited state atoms to the  ${}^3\mathrm{D}_J$  levels, which depletes the MOT atom number via decay to the  ${}^3\mathrm{P}_{0,2}$  and  ${}^1\mathrm{P}_1$  states that are dark to the cooling and imaging light.

In total, we record approximately 100 spectroscopy traces per transition, with about 40 frequency steps each, over the course of a few weeks. Exemplary spectroscopy curves are shown in Fig. 2. The model used for fitting the  ${}^{1}S_{0}\rightarrow{}^{3}P_{1}$  takes into account the recoil shift induced slight asymmetric lineshape. For the  ${}^{3}P_{1}\rightarrow{}^{3}D_{J}$  data, we fit a simple exponential model, which takes into account a small linear temporal drift of the atom number during the long measurement sequence. The lineshape models and systematic shifts including light and (residual) Zeeman shifts are discussed in appendices A and B.

Results—Taking into account all systematic shifts and correlations, we obtain the IS as  $\delta \nu^{A-A'} = \delta^{\star A}_{\rm cav} - \delta^{\star A'}_{\rm cav}$ , given in Tab. I. We resolve the IS at 2% to 11% of the

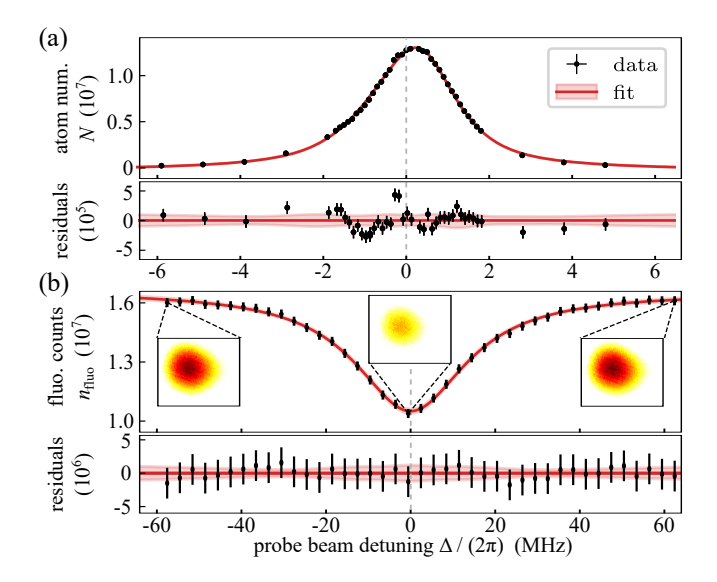


FIG. 2. Exemplary spectroscopy data on the (a)  ${}^{1}S_{0} \rightarrow {}^{3}P_{1}$  ( ${}^{200}\text{Hg}$ ) and (b)  ${}^{3}P_{1} \rightarrow {}^{3}D_{1}$  ( ${}^{202}\text{Hg}$ ) transitions in Hg. Atom numbers N and fluorescence counts  $n_{\text{fluo}}$  extracted from CCD images (see inset); the error bars include all systematic shifts and uncertainties. The  ${}^{1}S_{0} \rightarrow {}^{3}P_{1}$  fit model takes into account the asymmetry induced by the recoil shift of scattered probe beam photons. Minor residual deviations arise from a simplified steady-state optical Bloch solution neglecting Doppler broadening, which does not affect the line center. Dashed vertical lines mark the extracted atomic resonances.

natural linewidth, limited by systematic uncertainties. Uncertainties are lowest for highly abundant  $^{198}{\rm Hg}$  and  $^{202}{\rm Hg}$  and increase for less abundant pairs. Correlations show weak positive trends due to common systematic corrections. The IS between neighboring pairs (A'=A+2) averages to  $4.872\,89(2)\,{\rm GHz}$  for the intercombination and  $-361.7(2)\,{\rm MHz}$   $(-343.0(2)\,{\rm MHz})$  for the two  $^3{\rm P}_1{\to}^3{\rm D}_{1,\,2}$  lines. It increases approximately linearly with mass number, driven by the FS, while the MS remains approximately constant [34]. The exception being  $\delta\nu^{204-202}$  near the neutron shell closure, where the nucleus is sensitive to onsets of nuclear deformations (NDs) that induce the charge radii kink via FS contributions  $\propto\delta\langle r^2\rangle$  [54].

For the  ${}^{1}\mathrm{S}_{0} \rightarrow {}^{3}\mathrm{P}_{1}$  line, we improve measurement sensitivity by one to two orders of magnitude compared to Refs. [49, 61]. Latest comb-referenced Doppler-free saturation spectroscopy measurements in Refs. [49, 51] agree with our results to within  $\sim 2\sigma$ . To our knowledge, no prior ISS data or theoretical predictions exist for comparison with the  ${}^{3}\mathrm{P}_{1} \rightarrow {}^{3}\mathrm{D}_{J}$  spectroscopy data.

King Plot Analysis—To identify nuclear contributions and other subleading effects, we compare the mass-normalized ISs  $\overline{\delta\nu}_i^{A-A'}$  with  $\overline{x}^{A-A'} \equiv x^{A-A'}/\delta\mu^{A-A'}$  of two transitions i and j via a King plot (KP). For five isotopes and four isotope pairs, the associated IS vectors  $\overline{\delta\nu}_i$  span a four-dimensional space. Eliminating  $\delta\langle r^2\rangle$  in Eq. (1), the KP then yields a linear relation between ISs

on lines i and j to leading order,

$$\underline{\overline{\delta \nu}_{i} = F_{ij} \, \overline{\delta \nu}_{j} + K_{ij} \, \mathbb{1}} + \sum_{\kappa} G_{ij}^{(\kappa)} \, \overline{\delta \eta}_{(\kappa)} \,, \qquad (2)$$

where  $\mathbb{1} = (1,1,1,1)^{\mathsf{T}}$  denotes the vector of all ones,  $F_{ij} = F_i/F_j$  and  $X_{ij} = X_i - X_j F_{ij}$  for  $X \in [K,G]$ . Deviations from linearity reveal higher-order nuclear effects or BSM contributions. The separation of nuclear and electronic factors allow for comparison of vastly different electronic transitions, including comparisons to muonic atoms [36] and (highly-charged) ions [19, 21].

Given our and one additional ISS dataset for the  ${}^3P_2 \rightarrow {}^3S_1$  line from Ref. [47], six distinct two-dimensional KPs can be constructed; three of which are shown in Fig. 3. We apply orthogonal distance regression on the mass-normalized ISs  $\overline{\delta\nu}^{A-A'}$  of neighboring isotope pairs (A'=A+2) to check for KP-linearity. A pronounced nonlinearity is observed for the  ${}^1S_0 \rightarrow {}^3P_1$  to  ${}^3P_2 \rightarrow {}^3S_1$  KP, corresponding to a  $4.9\,\sigma$  rejection of the linear model  $(\chi^2_{\rm red}=14.7)$ . In contrast, the  ${}^3P_1 \rightarrow {}^3D_{1,2}$  to  ${}^1S_0 \rightarrow {}^3P_1$   $(\chi^2_{\rm red}=0.04$  and 1.00) and to  ${}^3P_2 \rightarrow {}^3S_1$   $(\chi^2_{\rm red}=0.04$  and 1.12) KPs are all consistent with linearity [65]. Any

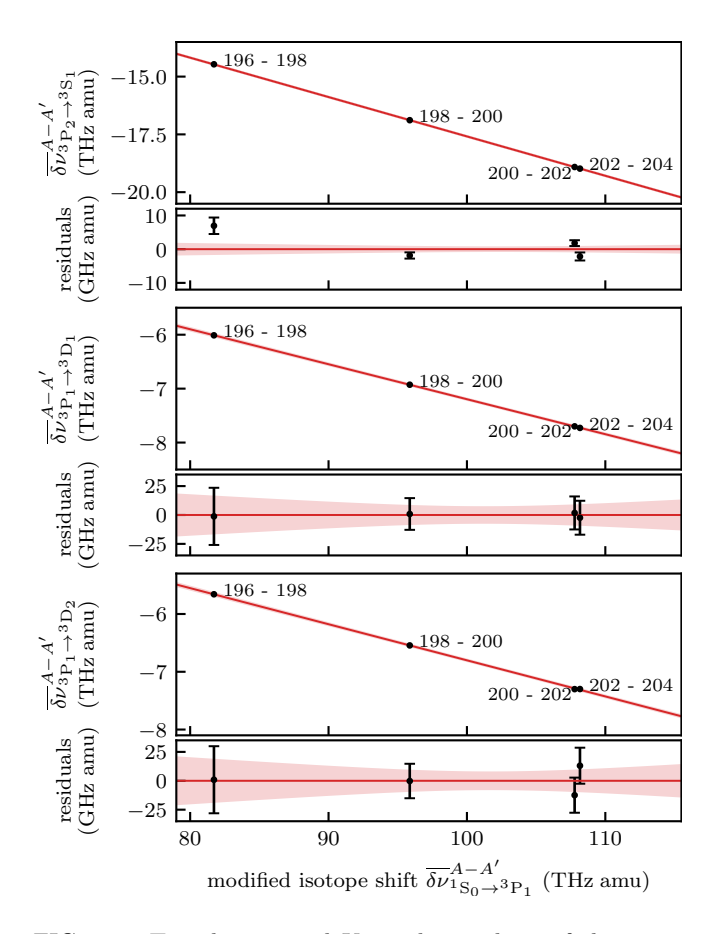


FIG. 3. Two-dimensional King plot analysis of the mass-normalized isotope shifts  $\overline{\delta\nu_i}^{A-A'} = \delta\nu_i^{A-A'}/\mu^{A-A'}$  with isotope pairs A' = A+2, revealing a 4.9 $\sigma$  nonlinearity in the  $^1\mathrm{S}_0 \! \to ^3\mathrm{P}_1 \rightleftharpoons {}^3\mathrm{P}_2 \! \to ^3\mathrm{S}_1$  comparison. Residuals are orthogonal distances to the linear fit.

$\overline{A}$	$p_{\mathrm{nat}}$ (%)	m (u)	$\delta \nu_{^{1}S_{0} \rightarrow ^{3}P_{1}}^{A-198}$				$\delta \nu_{^{3}\mathrm{P}_{1} \to ^{3}\mathrm{D}_{1}}^{A-198}$	$\delta\nu_{^{3}\mathrm{P}_{1}\rightarrow^{3}\mathrm{D}_{2}}^{A-198}$
			This work (kHz)	Ref. [49] (MHz)	Ref. [61] (MHz)	Ref. [35] (GHz)	This work (MHz)	This work (MHz)
196	0.15(1)	197.587 246(4)	+4179946(30)	_	_	+4.406	-307.49(98)	-289.4(1.2)
198	9.97(20)	199.6045762(7)	0(0)	0(0)	0(0)	0	0(0)	0(0)
200	23.10(19)	201.6219061(9)	-4805516(36)	-4806.28(33)	-4805(4)	-5.054	+347.24(58)	+328.02(62)
202	29.86(26)	203.6392358(12)	-10101224(22)	-10101.74(28)	-10102(4)	-10.579	+725.54(58)	+686.72(61)
204	6.87(15)	205.656 565 8(8)	-15311605(36)	-15312.02(30)	-15312(13)	-16.060	+1097.82(58)	+1038.31(63)
		$F (GHz/fm^2)$	$-52.22(30)^*$	-52.7(5.3)		-58.07(1.00)	+3.370(43)*	
		K  (THz amu)	$-2.43(55)^*$	4.0(1.2)		- 1.15(17)	$+3.42(35)$ † $-0.585(86)^*$ $-0.45(11)$ †	$+3.29(33)$ † $-0.440(95)^*$ $-0.31(12)$ †

TABLE I. Isotope shifts  $\delta\nu_i^{A-A'}$  on the  $i={}^1\mathrm{S}_0\to{}^3\mathrm{P}_1$  and  ${}^3\mathrm{P}_1\to{}^3\mathrm{D}_J$  (J=1,2) transitions as extracted from spectroscopy and in comparison to literature [35, 49, 61] where available. Uncertainties represent the combined statistical and systematic uncertainty of the analysis. In accordance with literature, only data for A'=198 are shown; full data and correlations are given in Ref. [62]. We also give the natural abundances  $p_{\mathrm{nat}}$  from Ref. [63] and compute the nuclear masses, m=M-Z  $m_e+E_b(A,Z)$ , with atomic masses M and binding energies  $E_b$  taken from Ref. [64]. The electronic FS (F) and MS (K) constants are extracted from KP comparisons to  $\overline{\delta\langle r^2\rangle}$  obtained from Ref. [52] (\*) or to  $\overline{\delta\nu_1}_{\mathrm{S_0}\to\mathrm{^3P_1}}$  with  $F_{\mathrm{1S_0}\to\mathrm{^3P_1}}$  extracted from theory in Ref. [35]  $(\dagger)$ .

potential higher-order nuclear or BSM effects align to the vectors of nuclear charge radius,  $\delta \langle r^2 \rangle$ , or inverse nuclear mass difference,  $\delta \mu$ , within the measurement uncertainty. Minor common residual deviations visible at (A, A') = (204, 202) could again hint at an onset of NDs towards the neutron rich isotopes. KP linearity is also indicated for the  $^3P_1 \rightarrow ^3D_1$  to  $^3P_1 \rightarrow ^3D_2$  KP ( $\chi^2_{\rm red} = 0.74$ ), which does not involve FS-sensitive s-states.

We extract the electronic FS  $(F_i)$  and MS  $(K_i)$  factors for the  ${}^3\mathrm{P}_1 \rightarrow {}^3\mathrm{D}_J$  lines from the slopes  $(F_{ij})$ , intercepts  $(K_{ij})$  and  $F_{{}^1\mathrm{S}_0 \rightarrow {}^3\mathrm{P}_1}$  given from electron structure calculations in Ref. [35]. Both lines show similar values, likely due to dominance of inner-shell contributions. We additionally extract  $F_i$ ,  $K_i$  for all lines from KP comparisons of the ISs to the mass-normalized nuclear charge radii differences,  $\overline{\delta\nu}_i \approx F_i \, \overline{\delta\langle r^2\rangle} + K_i \, \mathbb{1}$ , a direct result of Eq. (1). The charge radii are taken from optical, x-ray and muonic ISs, and electron scattering data in Ref. [52]. The resulting  ${}^3\mathrm{P}_1 \rightarrow {}^3\mathrm{D}_J$  KPs show good agreement with linearity. In contrast, the  ${}^1\mathrm{S}_0 \rightarrow {}^3\mathrm{P}_1$  and  ${}^3\mathrm{P}_2 \rightarrow {}^3\mathrm{S}_1$  KPs show small deviations  $(\chi^2_{\rm red} = 2.54, 3.14)$ , suggesting higher-order, s-state enhanced nuclear effects. The extracted  $F_i$  and  $K_i$  (see Tab. I) agree reasonably with theory [35, 49].

Generalized King Plot—To distinguish between higherorder nuclear and BSM contributions, we analyze the nonlinearity in a generalized King plot (GKP) [14, 26]. Following Eq. (2), two additional basis vectors  $\mathbf{\Lambda}_{\pm}$ , independent of the two linear KP directions ( $\mathbf{\Lambda}_{\pm} \notin \operatorname{span}(\overline{\delta \nu}_{j}, \mathbf{1})$ ), are sufficient to span the vector space. Any IS vector can then be expressed as the projection

$$\overline{\delta \nu}_i = F_{ij} \, \overline{\delta \nu}_j + K_{ij} \, \mathbb{1} + \lambda_+ \, \Lambda_+ + \lambda_- \, \Lambda_- \,. \tag{3}$$

Following the definition in Ref. [19], we choose

$$\mathbf{\Lambda}_{+} = (\overline{\delta\nu}_{j}^{c} - \overline{\delta\nu}_{j}^{b}, \ \overline{\delta\nu}_{j}^{a} - \overline{\delta\nu}_{j}^{d}, \ \overline{\delta\nu}_{j}^{d} - \overline{\delta\nu}_{j}^{a}, \ \overline{\delta\nu}_{j}^{b} - \overline{\delta\nu}_{j}^{c})^{\mathsf{T}}, 
\mathbf{\Lambda}_{-} = (\overline{\delta\nu}_{j}^{d} - \overline{\delta\nu}_{j}^{b}, \ \overline{\delta\nu}_{j}^{a} - \overline{\delta\nu}_{j}^{c}, \ \overline{\delta\nu}_{j}^{b} - \overline{\delta\nu}_{j}^{d}, \ \overline{\delta\nu}_{j}^{c} - \overline{\delta\nu}_{j}^{a})^{\mathsf{T}},$$

$$(4)$$

with isotope pairs  $a=(196,198),\ b=(198,200),\ c=(200,202),\ d=(202,204),$  and plot the resulting decomposition in Fig. 4. We compare the projections  $(\lambda_+,\lambda_-)$  with the characteristic nonlinearity shapes of potential higher-order corrections  $\propto \overline{\delta\eta}_{(\kappa)}$ , which form lines through the origin. The distance to the origin is determined by the associated electronic factors  $G_{ij}^{(\kappa)}$ . We consider QFS  $\propto \delta \langle r^2 \rangle^2$ , derived from charge

radii in Ref. [52], as a next leading order FS contri-While compared to Yb, nuclear quadrupole moment deformations in Hg are estimated to be small  $(\beta_2 \approx 0.094(1) [67])$  we also include energy corrections from a quadrupole-deformed Fermi model based on electron structure calculations of highly-charged ions,  $\propto \delta(\Delta E_{\rm tran,ND})$ , given in Ref. [43]. A rough estimate [68] of ND-induced contributions  $\propto \delta \langle r^4 \rangle$  is taken from Ref. [66], where charge radii moments of Hg are generated by a deep neural network trained on relativistic mean-field models and experimental data. Second-order  $MS \propto \delta(1/m^2) = 1/(m^A)^2 - 1/(m^{A'})^2$  is expected to be suppressed, but is also hard to distinguish from BSM interactions  $\propto (A-Z)$  in the GKP. At the current measurement resolution, GKP analyses of the  ${}^{3}P_{1} \rightarrow {}^{3}D_{J}$  data do not restrict any nonlinearity source. The  ${}^{3}P_{2} \rightarrow {}^{3}S_{1}$  to  ${}^{1}S_{0} \rightarrow {}^{3}P_{1}$  point however reproduces its 4.9 $\sigma$ -nonlinearity, that is not easily explained by theory predictions. While QFS, 2<sup>nd</sup>-order MS and BSM coupling can be rejected as a single nonlinearity source, multiple sources including ND or NP could still explain the observed nonlinearity.

Summary and Outlook—This work reports first obser-

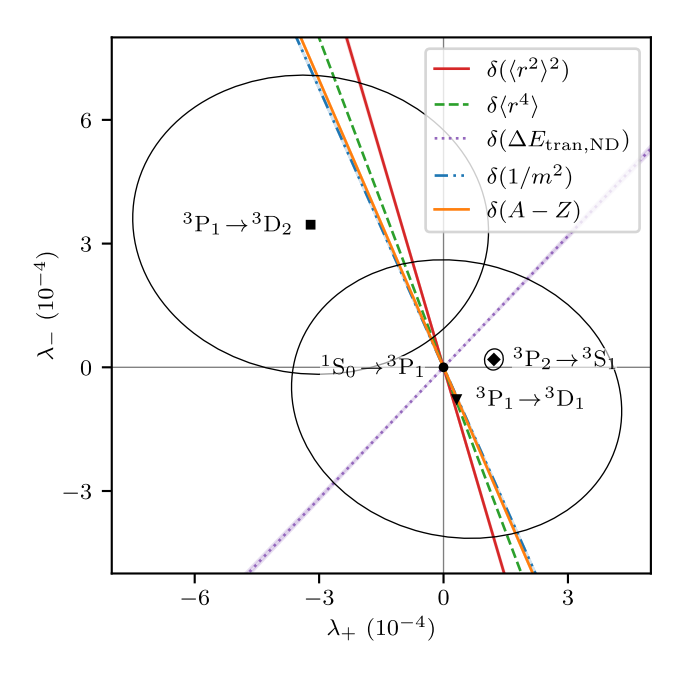


FIG. 4. Generalized King plot nonlinear decomposition analysis of the mass-normalized isotope shifts vectors  $\overline{\delta\nu_i}$  projected via  $(F_{ij},\,K_{ij},\,\lambda_+,\,\lambda_-)=(\overline{\delta\nu_j}\,\,\mathbbm{1}\,\,\Lambda_+\,\,\Lambda_-)^{-1}\cdot\overline{\delta\nu_j}$  via ISs of reference line  $j={}^1\mathrm{S}_0{\to}^3\mathrm{P}_1$  and vectors  $\Lambda_\pm$  given by Eq. (4). Higher order nuclear and BSM physics contribution vectors,  $\delta\eta_{(\kappa)}$ , show characteristic nonlinearity patterns that form lines through the origin with slopes  $\lambda_-/\lambda_+=-3.418(28)$  for QFS  $\propto\delta\langle r^2\rangle^2$  [52], -3(69) for ND  $\propto\delta\langle r^4\rangle$  [66], +1.061(15) for ND  $\propto\delta(\Delta E_{\mathrm{tran},\mathrm{ND}})$  from highly-charged ion calculations [43], -2.2542(5) for  $2^{\mathrm{nd}}$ -order MS  $\propto\delta(1/m^2)$  [66] and -2.3227(7) for BSM-coupling to a new boson  $\propto(A-Z)$ . The  $1\sigma$  uncertainty bands (shaded) are partially within the linewidth and omitted for ND  $\propto\delta\langle r^4\rangle$  to improve visibility.

vation of KP nonlinearity in neutral Hg at the  $20\,\mathrm{kHz}$  level, revealing sensitivity to higher-order nuclear effects relevant for tests of fundamental interactions. Although current precision and theory predictions limit the GKP interpretation, advancing electronic structure calculations alongside refined ND predictions, as demonstrated for Yb, will enable nuclear  $G_i^{(\kappa)}$  and new physics  $X_i$  coupling estimates, turning Hg ISS into a measurement of nuclear structure and a firm bound on BSM physics.

Future gain in sensitivity will come from improved spectroscopy resolution on existing transitions or adding at least one (dipole-allowed) line with comparable uncertainty. BSM searches will strongly benefit from accessing ultra-narrow clock transitions such as the  ${}^{1}S_{0} \rightarrow {}^{3}P_{0,2}$  lines at 265.6 nm and 227 nm [69–73]. These dipole-forbidden transitions, weakly enabled via hyperfine or field-induced mixing, offer Hz-level linewidths and could be driven either directly or via multi-photon schemes [71] with available laser technology. This also opens prospects to a closed IS cycle ( ${}^{1}S_{0} \rightarrow {}^{3}P_{1}$ ,  ${}^{3}P_{1} \rightarrow {}^{3}S_{1}$ ,  ${}^{3}S_{1} \rightarrow {}^{3}P_{2}$ , and  ${}^{3}P_{2} \rightarrow {}^{1}S_{0}$ ) that would provide stringent internal tests of SM and BSM interpretations.

Note added—While finalizing this manuscript, we became aware of related work by Gravina et al. [51], which reports similar measurements on  ${}^{1}S_{0} \rightarrow {}^{3}P_{1}$  using a different approach. Our study was conducted independently.

Acknowledgments—We thank Q. Lavigne for contributions to the early stages of the experimental setup and spectroscopy measurements. We thank B. Ohayon, J. Berengut, S. Heider, and A. Reuß for fruitful discussions. Financial support from the DFG through SFB/TR185 "OSCAR" (Project No. 277625399), as well as from the ERC "quMercury" (Project No. 757386) and "UVQuanT" (Project No. 101080164) is gratefully acknowledged.

Data availability—The data that support the findings of this work are openly available [62]. Additional data are available upon reasonable request from the authors.

- \* Contact author: groh@physik.uni-bonn.de
- [1] S. M. Brewer, J.-S. Chen, A. M. Hankin, E. R. Clements, C. W. Chou, D. J. Wineland, D. B. Hume, and D. R. Leibrandt, <sup>27</sup>Al<sup>+</sup> quantum-logic clock with a systematic uncertainty below 10<sup>-18</sup>, Phys. Rev. Lett. **123**, 033201 (2019).
- [2] A. Aeppli, K. Kim, W. Warfield, M. S. Safronova, and J. Ye, Clock with  $8\times10^{-19}$  systematic uncertainty, Phys. Rev. Lett. **133**, 023401 (2024).
- [3] W. F. McGrew et al., Atomic clock performance enabling geodesy below the centimetre level, Nature 564, 87 (2018).
- [4] C. G. Parthey et al., Improved measurement of the hydrogen 1S-2S transition frequency, Phys. Rev. Lett. 107, 203001 (2011).
- [5] A. Matveev et al., Precision measurement of the hydrogen 1S-2S frequency via a 920-km fiber link, Phys. Rev. Lett. 110, 230801 (2013).
- [6] X. Fan, T. G. Myers, B. A. D. Sukra, and G. Gabrielse, Measurement of the electron magnetic moment, Phys. Rev. Lett. 130, 071801 (2023).
- [7] D. Hanneke, S. Fogwell, and G. Gabrielse, New measurement of the electron magnetic moment and the fine structure constant, Phys. Rev. Lett. 100, 120801 (2008).
- [8] M. S. Safronova, D. Budker, D. DeMille, D. F. J. Kimball, A. Derevianko, and C. W. Clark, Search for new physics with atoms and molecules, Rev. Mod. Phys. 90, 025008 (2018).
- [9] T. S. Roussy et al., Experimental constraint on axionlike particles over seven orders of magnitude in mass, Phys. Rev. Lett. 126, 171301 (2021).
- [10] A. Derevianko and M. Pospelov, Hunting for topological dark matter with atomic clocks, Nat. Phys. 10, 933 (2014).
- [11] I. Counts, J. Hur, D. P. L. Aude Craik, H. Jeon, C. Leung, J. C. Berengut, A. Geddes, A. Kawasaki, W. Jhe, and V. Vuletić, Evidence for nonlinear isotope shift in Yb<sup>+</sup> search for new boson, Phys. Rev. Lett. 125, 123002 (2020).
- [12] N. L. Figueroa, J. C. Berengut, V. A. Dzuba, V. V. Flambaum, D. Budker, and D. Antypas, Precision determina-

- tion of isotope shifts in ytterbium and implications for new physics, Phys. Rev. Lett. **128**, 073001 (2022).
- [13] K. Ono, Y. Saito, T. Ishiyama, T. Higomoto, T. Takano, Y. Takasu, Y. Yamamoto, M. Tanaka, and Y. Takahashi, Observation of nonlinearity of generalized King plot in the search for new boson, Phys. Rev. X 12, 021033 (2022).
- [14] J. Hur et al., Evidence of two-source King plot nonlinearity in spectroscopic search for new boson, Phys. Rev. Lett. 128, 163201 (2022).
- [15] M. Door et al., Probing new bosons and nuclear structure with ytterbium isotope shifts, Phys. Rev. Lett. 134, 063002 (2025).
- [16] T. Ishiyama, K. Ono, H. Kawase, T. Takano, R. Asano, A. Sunaga, Y. Yamamoto, M. Tanaka, and Y. Takahashi, Orders-of-magnitude improved precision spectroscopy of an inner-shell orbital clock transition in neutral ytterbium (2025), arXiv:2505.04154 [physics.atom-ph].
- [17] F. Gebert, Y. Wan, F. Wolf, C. N. Angstmann, J. C. Berengut, and P. O. Schmidt, Precision isotope shift measurements in calcium ions using quantum logic detection schemes, Phys. Rev. Lett. 115, 053003 (2015).
- [18] D. Röser, L. Möller, H. Keßler, and S. Stellmer, Isotopeshift measurement of the 423-nm transition in neutral Ca, Phys. Rev. A 110, 032809 (2024).
- [19] A. Wilzewski et al., Nonlinear calcium king plot constrains new bosons and nuclear properties, Phys. Rev. Lett. 134, 233002 (2025).
- [20] S. Hofsäss, J. E. Padilla-Castillo, S. C. Wright, S. Kray, R. Thomas, B. G. Sartakov, B. Ohayon, G. Meijer, and S. Truppe, High-resolution isotope-shift spectroscopy of Cd I, Phys. Rev. Res. 5, 013043 (2023).
- [21] N.-H. Rehbehn, M. K. Rosner, J. C. Berengut, P. O. Schmidt, T. Pfeifer, M. F. Gu, and J. R. C. López-Urrutia, Narrow and ultranarrow transitions in highly charged Xe ions as probes of fifth forces, Phys. Rev. Lett. 131, 161803 (2023).
- [22] C. Delaunay, R. Ozeri, G. Perez, and Y. Soreq, Probing atomic Higgs-like forces at the precision frontier, Phys. Rev. D 96, 093001 (2017).
- [23] J. C. Berengut et al., Probing new long-range interactions by isotope shift spectroscopy, Phys. Rev. Lett. 120, 091801 (2018).
- [24] A. J. Krasznahorkay et al., Observation of anomalous internal pair creation in <sup>8</sup>Be: a possible indication of a light, neutral boson, Phys. Rev. Lett. 116, 042501 (2016).
- [25] J. L. Feng, B. Fornal, I. Galon, S. Gardner, J. Smolinsky, T. M. P. Tait, and P. Tanedo, Protophobic fifth-force interpretation of the observed anomaly in <sup>8</sup>Be nuclear transitions, Phys. Rev. Lett. 117, 071803 (2016).
- [26] J. C. Berengut and N. S. Oreshkina, Second-order hyperfine structure and its impact on searches for new physics using isotope-shift spectroscopy, Phys. Rev. A 112, 022804 (2025).
- [27] C. Solaro, S. Meyer, K. Fisher, J. C. Berengut, E. Fuchs, and M. Drewsen, Improved isotope-shift-based bounds on bosons beyond the standard model through measurements of the  $^2\mathrm{D}_{3/2}-^2\mathrm{D}_{5/2}$  interval in Ca<sup>+</sup>, Phys. Rev. Lett. **125**, 123003 (2020).
- [28] T. T. Chang, B. B. Awazi, J. C. Berengut, E. Fuchs, and S. C. Doret, Systematic-free limit on new light scalar bosons via isotope-shift spectroscopy in Ca<sup>+</sup>, Phys. Rev. A 110, 1030801 (2024).
- [29] M. Bordag, G. L. Klimchitskaya, U. Mohideen, and V. M.

- Mostepanenko, Advances in the Casimir effect, edited by G. L. Klimchitskaya and [more], International Series of Monographs on Physics Ser., Vol. 145 (Oxford University Press, Oxford, 2009) pp. 1–768.
- [30] J. A. Grifols, E. Massó, and S. Peris, Energy loss from the sun and red giants: bounds on short-range baryonic and leptonic forces, Mod. Phys. Lett. A 04, 311 (1989).
- [31] G. Raffelt, Limits on a CP-violating scalar axion-nucleon interaction, Phys. Rev. D 86, 015001 (2012).
- [32] V. V. Nesvizhevsky, G. Pignol, and K. V. Protasov, Neutron scattering and extra-short-range interactions, Phys. Rev. D 77, 034020 (2008).
- [33] C. Delaunay, C. Frugiuele, E. Fuchs, and Y. Soreq, Probing new spin-independent interactions through precision spectroscopy in atoms with few electrons, Phys. Rev. D 96, 115002 (2017).
- [34] X. Zhang, B.-Q. Lu, J.-G. Li, and H.-X. Zou, Theoretical investigation on hyperfine structure and isotope shift for  $5d^{10}$  6s  $^2S_{1/2}$   $5d^9$  6s  $^2D_{5/2}$  clock transition in Hg<sup>+</sup>, Acta Phys. Sin-ch. Ed. **68**, 043101 (2019).
- [35] J. S. Schelfhout and J. J. McFerran, Multiconfiguration Dirac-Hartree-Fock calculations for Hg and Cd with estimates for unknown clock-transition frequencies, Phys. Rev. A 105, 022805 (2022).
- [36] W. H. King, Isotope shifts in atomic spectra, Physics of Atoms and Molecules Ser. (Springer, New York, NY, 1984).
- [37] J. C. Berengut, C. Delaunay, A. Geddes, and Y. Soreq, Generalized King linearity and new physics searches with isotope shifts, Phys. Rev. Res. 2, 043444 (2020).
- [38] J. A. R. Griffith, G. R. Isaak, R. New, M. P. Ralls, and C. P. van Zyl, Anomalies in the optical isotope shifts of samarium, J. Phys. B: At. Mol. Phys. 12, L1 (1979).
- [39] J. A. R. Griffith, G. R. Isaak, R. New, and M. P. Ralls, Anomalies in the optical isotope shifts of samarium, J. Phys. B: At. Mol. Phys. 14, 2769 (1981).
- [40] C. W. P. Palmer and D. N. Stacey, Theory of anomalous isotope shifts in samarium, J. Phys. B: At. Mol. Phys. 15, 997 (1982).
- [41] H. Haber, G. Kane, and T. Sterling, The fermion mass scale and possible effects of higgs bosons on experimental observables, Nuclear Physics B 161, 493 (1979).
- [42] S. Ebata and T. Nakatsukasa, Octupole deformation in the nuclear chart based on the 3D Skyrme Hartree-Fock plus BCS model, Phys. Scripta 92, 064005 (2017).
- [43] Z. Sun, I. A. Valuev, and N. S. Oreshkina, Nuclear deformation effects in the spectra of highly charged ions, Phys. Rev. Res. 6, 023327 (2024).
- [44] J. Blaise and H. Chantrel, Structures hyperfines de raies du spectre d'arc du mercure et moment quadrupolaire de <sup>201</sup>Hg, J. Phys. Radium 18, 193 (1957).
- [45] S. Gerstenkorn, J. J. Labarthe, and J. Vergès, Fine and hyperfine structures and isotope shifts in the arc spectrum of mercury. Part I. Experimental study of the infrared spectrum by fourier transform spectroscopy, Phys. Scripta 15, 167 (1977).
- [46] M. Kroll, Saturation spectroscopy and resonant degenerate four-wave mixing in Hg at 546.1 nm, Opt. Lett. 7, 151 (1982).
- [47] M. D. Rayman, C. G. Aminoff, and J. L. Hall, Precise laser frequency scanning using frequency-synthesized optical frequency sidebands: application to isotope shifts and hyperfine structure of mercury, J. Opt. Soc. Am. B 6, 539 (1989).

- [48] C. J. Sansonetti and D. Veza, Doppler-free measurement of the 546 nm line of mercury, J. Phys. B: At. Mol. Opt. Phys. 43, 205003 (2010).
- [49] M. Witkowski, G. Kowzan, R. Munoz-Rodriguez, R. Ciuryło, P. S. Żuchowski, P. Masłowski, and M. Zawada, Absolute frequency and isotope shift measurements of mercury  ${}^{1}s_{0} {}^{3}p_{1}$  transition, Opt. Express **27**, 11069 (2019).
- [50] S. Gravina, N. A. Chishti, S. Di Bernardo, E. Fasci, A. Castrillo, A. Laliotis, and L. Gianfrani, Combreferenced doppler-free spectrometry of the <sup>200</sup>Hg and <sup>202</sup>Hg intercombination line at 254 nm, Phys. Rev. Lett. 132, 213001 (2024).
- [51] S. Gravina, A. Castrillo, and L. Gianfrani, Isotope shift spectroscopy in mercury vapors: a valid alternative to ytterbium for new physics search (2025), arXiv:2509.08622 [physics.atom-ph].
- [52] I. Angeli and K. P. Marinova, Table of experimental nuclear ground state charge radii: An update, Atom. Data Nucl. Data 99, 69 (2013).
- [53] G. Ulm et al., Isotope shift of <sup>182</sup>Hg and an update of nuclear moments and charge radii in the isotope range <sup>181</sup>Hg - <sup>206</sup>Hg, Zeitschrift für Physik A Atomic Nuclei 325, 247 (1986).
- [54] T. Day Goodacre, Developments of the ISOLDE RILIS for radioactive ion beam production and the results of their application in the study of exotic mercury isotopes, Ph.D. thesis, The University of Manchester (2017).
- [55] S. M. C. Sels, Laser spectroscopy of neutron-deficient mercury isotopes and commissioning of a gas-jet based RFQ ion guide, Ph.D. thesis, Leuven University (2018).
- [56] S. Sels et al., Shape staggering of midshell mercury isotopes from in-source laser spectroscopy compared with density-functional-theory and Monte Carlo shell-model calculations, Phys. Rev. C 99, 044306 (2019).
- [57] T. Day Goodacre *et al.*, Laser spectroscopy of neutron-rich  $^{207,208}$ Hg isotopes: Illuminating the kink and odd-even staggering in charge radii across the N=126 shell closure, Phys. Rev. Lett. **126**, 032502 (2021).
- [58] B. A. Marsh et al., Characterization of the shapestaggering effect in mercury nuclei, Nat. Phys. 18, 219 (2022).
- [59] Q. Lavigne, T. Groh, and S. Stellmer, Magneto-optical trapping of mercury at high phase-space density, Phys. Rev. A 105, 033106 (2022).
- [60] M. Büki, D. Röser, and S. Stellmer, Frequencyquintupled laser at 308 nm for atomic physics applications, Appl. Optics 60, 9915 (2021).
- [61] W. G. Schweitzer, Hyperfine structure and isotope shifts in the 2537-Å line of mercury by a new interferometric method, J. Opt. Soc. Am. 53, 1055 (1963).
- [62] T. Groh and S. Stellmer, Data: Probing nuclear interactions through isotope shift spectroscopy of mercury, 10.5281/zenodo.17337558 (2025).
- [63] J. S. Coursey, D. J. Schwab, J. J. Tsai, and R. A. Dragoset, Atomic weights and isotopic compositions (version 4.1), National Institute of Standards and Technology, Gaithersburg, MD. (2015).
- [64] M. Wang, W. J. Huang, F. G. Kondev, G. Audi, and S. Naimi, The AME 2020 atomic mass evaluation (II). tables, graphs and references, Chinese Phys. C 45, 030003 (2021).
- [65] The low  $\chi^2_{\rm red}$  values indicate overfitting and therefore no

- statistical tension to the linear model within the uncertainties.
- [66] T. S. Shang, H. H. Xie, J. Li, and H. Liang, Global prediction of nuclear charge density distributions using a deep neural network, Phys. Rev. C 110, 014308 (2024).
- [67] B. Pritychenko, M. Birch, B. Singh, and M. Horoi, Tables of E2 transition probabilities from the first 2<sup>+</sup> states in even-even nuclei, Atomic Data and Nuclear Data Tables 107, 1 (2016).
- [68] We assume a charge radius uncertainty of 0.02 fm from Fig. 2 in Ref. [66] and propagate the uncertainty to  $\delta \langle r^4 \rangle$ .
- [69] R. Tyumenev et al., Comparing a mercury optical lattice clock with microwave and optical frequency standards, New J. Phys. 18, 113002 (2016).
- [70] S. G. Porsev, U. I. Safronova, and M. S. Safronova, Theoretical study of the g factor and lifetime of the 6s 6p  $^3$ P<sub>0</sub> state of mercury, Phys. Rev. A **96**, 012509 (2017).
- [71] E. A. Alden, K. R. Moore, and A. E. Leanhardt, Twophoton E1-M1 optical clock, Phys. Rev. A 90, 012523 (2014).
- [72] A. Taichenachev, V. Yudin, C. Oates, C. Hoyt, Z. Barber, and L. Hollberg, Magnetic field-induced spectroscopy of forbidden optical transitions with application to latticebased optical atomic clocks, Phys. Rev. Lett. 96, 083001 (2006).
- [73] R. Santra, E. Arimondo, T. Ido, C. H. Greene, and J. Ye, High-accuracy optical clock via three-level coherence in neutral bosonic 88 Sr, Phys. Rev. Lett. 94, 173002 (2005).
- [74] J. Gäßler, G. Quast, D. Savoiu, and C. Verstege, kafe2 A Modern Tool for Model Fitting in Physics Lab Courses (2022), arXiv:2210.12768 [physics.ed-ph].
- [75] R. Brun et al., root-project/root: v6-36-04 (2025).

Appendix A: Systematics—The systematic shifts and their corrections for the determination of the atomic resonances with respect to the cavity lines,  $\delta_{\text{cav}}^{\star A}$ , are mostly common mode between isotopes and cancel in the computation of the ISs. The dominant sources of systematic shift are probe recoil induced Doppler shifts, AC Stark light shifts, Zeeman shifts, and the slow drift of the reference cavity. Uncertainties quoted in Tab. II are conservative upper bounds, due to correlations or limited ability to isolate individual effects.

We characterize and correct all systematics based on direct calibration measurements, supported by (numerical) models. Residual recoil and light shifts are corrected with calibration measurements based on probe intensity  $I_{\rm probe}$  and show small isotope dependence (scaling slightly with nuclear mass). Off-resonant light shifts are estimated for both probe and MOT beams. For  ${}^{1}{\rm S}_{0} \rightarrow {}^{3}{\rm P}_{1}$  (detected in free-fall), stray MOT light is negligible due to fast shuttering. For  ${}^{3}{\rm P}_{1} \rightarrow {}^{3}{\rm D}_{J}$  (in-MOT spectroscopy), MOT-induced shifts and fluctuations are measured as a function of beam power and detuning.

Zeeman shifts arise from (residual) magnetic gradient fields; for  ${}^3\mathrm{P}_1{\to}{}^3\mathrm{D}_J$  we operate the MOT at  ${\sim}0.1\,\mathrm{T/m}$ . Numerical modeling and data analysis confirm shift suppression except for  ${}^{196}\mathrm{Hg}$  detected at higher MOT gradients. Cavity drift is corrected by a linear fit of atomic resonance to cavity detuning over time, as discussed above.

	Systematic	Correction	Shift (kHz)
$^{1}\mathrm{S}_{0}$ $\rightarrow$ $^{3}\mathrm{P}_{1}$	Probe recoil Zeeman shift Reference drift Probe frequency Doppler shift Light shift $N$ fluctuations $N$ determination	$\begin{aligned} &a_I^A  I_{\text{probe}} \\ &\text{numerical model} \\ &4  a_{\text{cav}}  t  \left( t \approx 22  \text{days} \right) \\ &\pm \Delta f_{\text{probe}} \\ &\pm \Delta f_{\text{Doppler}} \\ &\pm \Delta f_{\text{light}} \\ &\pm \Delta N \\ &\pm \Delta N_{od} \end{aligned}$	$\begin{array}{c} 33(15) \\ -5(15) \\ 1517(34) \\ 0(22) \\ 0(20) \\ 0(0) \\ 0(15) \\ 0(5) \\ \end{array}$
$^3\mathrm{P}_1{ ightarrow}^3\mathrm{D}_J$	Light shift   Zeeman shift   Probe recoil   Reference drift   Probe frequency $N$ drift	$\begin{split} &\delta\nu_{\rm light}(\Delta_{\rm mot},P_{\rm mot})\\ &a_B\partial_z B + b_B\\ &\delta\nu_{\rm probe}\\ &5a_{\rm cav}t(t\approx 9{\rm h})\\ &\pm\Delta f_{\rm probe}\\ &\pm\Delta N \end{split}$	$\begin{array}{c} 3900(170) \\ -560(810)^{\dagger} \\ 0(220) \\ 0(150) \\ 26(1) \\ 0(15) \\ 0(70) \end{array}$

TABLE II. Upper limits for the systematic shifts and uncertainties in determination of the  ${}^{1}\mathrm{S}_{0} \rightarrow {}^{3}\mathrm{P}_{1}$  and  ${}^{3}\mathrm{P}_{1} \rightarrow {}^{3}\mathrm{D}_{J}$  (J=1,2) resonance locations,  $\delta_{\mathrm{cav}}^{\star A}$ . Uncertainties represent  $1\sigma$  combined standard uncertainties. Entries marked with  $\dagger$  apply only to isotope  ${}^{196}\mathrm{Hg}$ .

Laser lock errors and probe frequency instabilities are conservatively estimated using (in-loop) error signals and error statistics from repeated scans. Atom number uncertainties and extraction (e.g., optical density fit error) are included as nuisance errors.

Background gas and Hg-Hg collisional shifts are negligible at the low background gas pressure of  $<1\times10^{-9}\,\rm mbar$  in the ultra-high vacuum environment of the MOT. Residual Doppler shifts from atomic motion are minimized by balancing MOT beam powers and aligning the probe orthogonal to gravity, limiting systematic shifts to below 20 kHz and isotope-dependent effects to under 100 Hz/amu. Other broadening mechanisms, such as Doppler and transit-time effects, do not shift the line center positions and add only minor uncertainty to the atomic resonance extraction.

Appendix B: Lineshape—For fitting of the  ${}^{1}S_{0}\rightarrow{}^{3}P_{1}$  spectroscopy data the lineshape model needs to take into account the asymmetry induced by the recoil shift of scattered probe beam photons. For this we numerically de-

termine the number of scattered photons  $n_{\rm scat}$  (4 to 15 photons on resonance,  $\Delta=0$ ) in dependence of the probe beam detuning  $\Delta$ ,

$$n_{\rm scat}(\Delta) = \left( n \mid \int_{0}^{n-1} di \, \frac{1}{R_{\rm scat}(\Delta + i \, \Delta_{\rm rec})} \stackrel{!}{=} t_{\rm exp} \right), \quad (5)$$

where we assume a photon scattering rate of

$$R_{\rm scat}(\Delta) = \frac{\Gamma}{2} \frac{s_0}{1 + s_0 + (2\Delta/\Gamma)^2}.$$
 (6)

 $\Delta_{\rm rec}$  is the single-photon recoil shift. The spectroscopy fit of  $N \propto n_{\rm scat}$  versus frequency, extends Eq. (5) by introducing a variable amplitude and offset.

For the  ${}^3\mathrm{P}_1 \rightarrow {}^3\mathrm{D}_J$  spectroscopy the probe beam depletes the MOT atom number. Assuming probe beam dominated atom loss and neglecting Doppler broadening, the loss rate is given by  $R_{\mathrm{loss}}(\Delta) = \beta_{\mathrm{loss}} R_{\mathrm{scat}}(\Delta)$  with  $\beta_{\mathrm{loss}}$  the branching ratio to metastable states. The atom number then decays as  $N(t) \propto e^{-R_{\mathrm{loss}}(\Delta) t}$  and the detected fluorescence is given by the integral over the time,  $n_{\mathrm{fluo}}(\Delta) \propto \int_0^{t_{\mathrm{exp}}} N(t) \, \mathrm{d}t$ . To account for slow drift in atom number due to MOT cooling power variations, we add a linear background term  $\propto a_n \cdot \Delta$ , and obtain

$$n_{\text{fluo}}(\Delta) = (n_0 + a_n \Delta) \left[ 1 + (2 \Delta/\Gamma)^2 \right]$$

$$\left[ 1 - \exp\left(-\frac{a}{1 + (2 \Delta/\Gamma)^2}\right) \right]. \tag{7}$$

The additional systematic uncertainty of this drift is estimated to be  $70\,\mathrm{kHz}$ . We validate both fit models against pure Lorentzian, Gaussian, and Voigt profiles, which in comparison reduce fit quality and introduce overfitting or parameter correlations.

The fits take into account all systematic shifts, uncertainties, and their correlations. All confidence interval estimations in this work are performed via the kafe2 python toolbox [74] which interfaces the Minuit2 C++ library maintained by the CERN ROOT team [75].